SURFACE PLASMON POLARITON DEPENDENCE ON METAL SURFACE MORPHOLOGY

Robert E. Peale

University of Central Florida
4000 Central Florida Boulevard
Orlando, FL 32816-8005

13 November 2007

Final Report

AIR FORCE RESEARCH LABORATORY
Sensors Directorate
Electromagnetics Technology Division
80 Scott Drive
Hanscom AFB MA 01731-2909

NOTICE AND SIGNATURE PAGE

This report was cleared for public release by the Electronic Systems Center Public Affairs Office for the Air Force Research Laboratory Electromagnetic Technology Division and is available to the general public, including foreign nationals. Copies may be obtained from the Defense Technical Information Center (DTIC) (http://www.dtic.mil).

AFRL-RY-HS-TR-2007-0030 HAS BEEN REVIEWED AND IS APPROVED FOR PUBLICATION IN ACCORDANCE WITH ASSIGNED DISTRIBUTION STATEMENT.

/signature/

WALTER BUCHWALD
Contract Monitor
Electromagnetic Technology Branch

/signature/

JOSEPH P. LORENZO
Chief
Electromagnetic Technology Branch

/signature/

MICHAEL N. ALEXANDER
Technical Advisor
Electromagnetic Technology Division

This report is published in the interest of scientific and technical information exchange, and its publication does not constitute the Government's approval or disapproval of its ideas or findings.

REPORT DOCUMENTATION PAGE

1. REPORT DATE *(DD-MM-YYYY)* 13-11-2007	2. REPORT TYPE FINAL REPORT	3. DATES COVERED *(From - To)* 30 Nov 2006 – 31 Jul 2007

4. TITLE AND SUBTITLE

Surface Plasmon Polariton Dependence on Metal Surface Morphology

5a. CONTRACT NUMBER
FA8718-06-C-0076

5b. GRANT NUMBER

5c. PROGRAM ELEMENT NUMBER
61102F

6. AUTHOR(S)

Robert E. Peale

5d. PROJECT NUMBER
2305

5e. TASK NUMBER
HC

5f. WORK UNIT NUMBER
0B

7. PERFORMING ORGANIZATION NAME(S) AND ADDRESS(ES)
University of Central Florida
4000 Central Boulevard
Orlando, FL 32816-8005

8. PERFORMING ORGANIZATION REPORT

9. SPONSORING / MONITORING AGENCY NAME(S) AND ADDRESS(ES)
Electromagnetics Technology Division
Sensors Directorate
Air Force Research Laboratory
80 Scott Drive
Hanscom AFB MA 01731-2909

10. SPONSOR/MONITOR'S ACRONYM(S)
AFRL-RY-HS

11. SPONSOR/MONITOR'S REPORT NUMBER(S)
AFRL-RY-HS-TR-2007-0030

12. DISTRIBUTION / AVAILABILITY STATEMENT

APPROVED FOR PUBLIC RELEASE; DISTRIBUTION UNLIMITED

13. SUPPLEMENTARY NOTES
Cleared for Public Release by ESC/PA: ESC 07-1302, dated 7 November 2007

14. ABSTRACT

Generation and propagation of surface plasmons on nano-structured gold films was studied using optical and electron-beam techniques. Optical excitation of surface plasmons in "Au-black" films prepared by evaporation in moderate vacuum was observed. Initial indication of propagation of surface plasmons at visible-light frequencies over ~10 nm length scales was observed. A tunable terahertz detector based on two-dimensional plasmons in a semiconductor heterostructure was designed. These results have application to the characterization of the complex permittivity of absorbing films for terahertz bolometers and to the development of a terahertz spectrometer on a chip, both of which are relevant to terahertz remote chemical and biological sensing.

15. SUBJECT TERMS
Surface Plasmon, permittivity, gold black, two-dimensional electron gas, detector, terahertz, far infrared

16. SECURITY CLASSIFICATION OF:			17.LIMITATION OF ABSTRACT	18.NUMBER OF PAGES	19a. NAME OF RESPONSIBLE PERSON Walter Buchwald
a. REPORT Unclassified	**b. ABSTRACT** Unclassified	**c. THIS PAGE** Unclassified	SAR	39	**19b. TELEPHONE NUMBER** *(include area code)* 781-377-7400

TABLE OF CONTENTS

LIST OF FIGURES

iv

1. Introduction

Generation and propagation of surface plasmons on nano-structured gold films was studied using optical and electron-beam techniques. Optical excitation of surface plasmons in "Au-black" films prepared by evaporation in moderate vacuum was observed. Indication of frequency-dependent propagation of surface plasmons at visible-light frequencies over submicron length scales was observed.

A tunable terahertz detector based on two-dimensional plasmons in a semiconductor heterostructure was designed. These results have application to the characterization of the complex permittivity of absorbing films for terahertz bolometers and to the development of a terahertz spectrometer on a chip, both of which are relevant to terahertz remote sensing of chem/bio agents.

2. Surface Plasmons

2.1 Gold-black

Gold-black is nano-structured interconnected gold particles deposited by evaporation on a substrate in a standard thermal evaporator in an inert gas ambient at pressures of ~1 Torr. At these pressures, evaporated gold atoms undergo collisions and limited condensation before they settle on the substrate, resulting in a low density nano-structured film characterized by strong absorption from visible to far-infrared regions of the spectrum. Such films have been used extensively as coatings for far-infrared bolometers. The author is separately funded by Zyberwear, Inc. to prepare and optimize such coatings for bolometer applications. Fig. 1 is a representative scanning electron microscope image of one of the prepared gold-black samples.

The absorption properties of Au-black are fundamentally related to its complex permittivity. A goal of this AFRL-funded study is to determine if resonant excitation of

surface plasmons by optical beams can be used to determine the complex permittivity of gold black films.
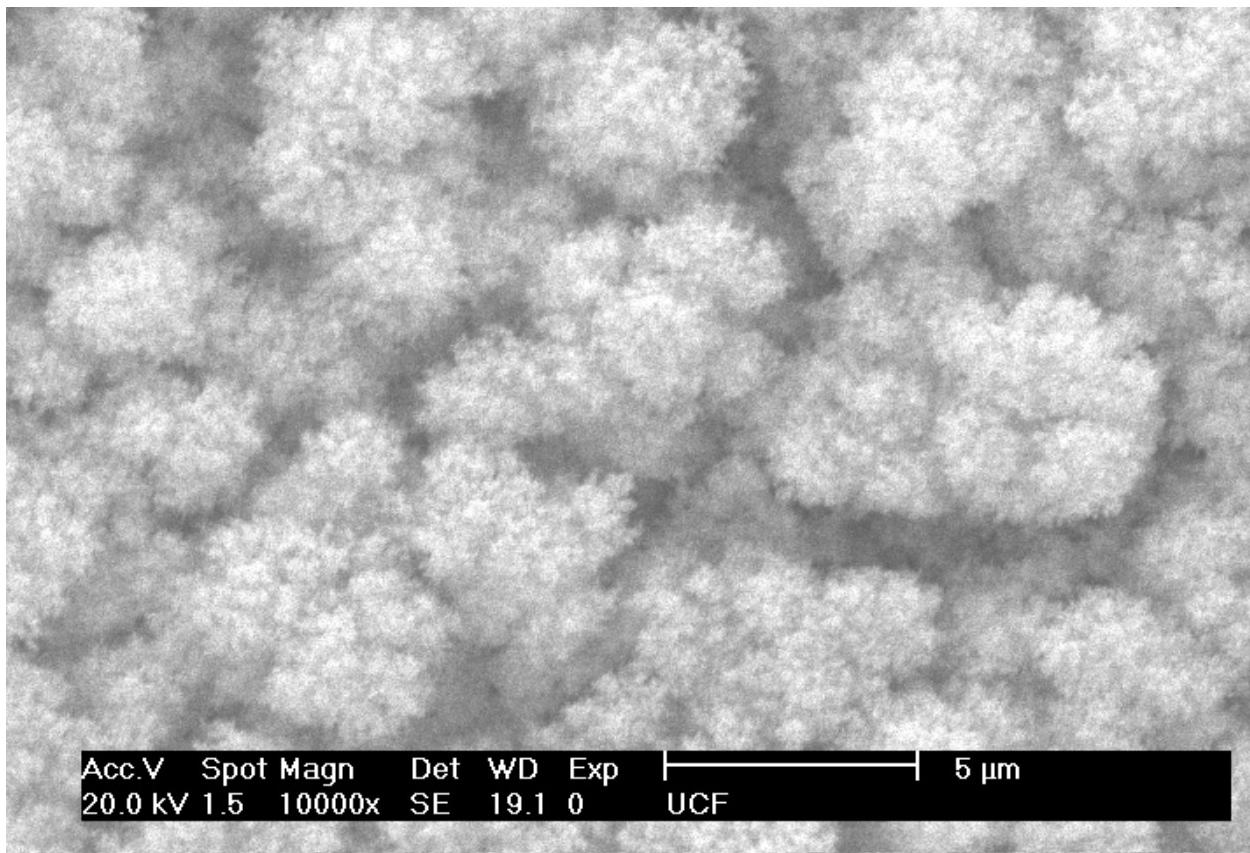
Figure 1: SEM-image of Au-black film

2.2 Optical measurements

Surface Plasmon Polaritons (SPP) are inhomogeneous electromagnetic plane waves bound to the surface of a conductor. Knowledge of SPP characteristics is of timely and critical interest to the rapidly expanding field of SPP-based "Plasmonics." Practical interest derives from the possibility of nano-scale optoelectronic devices, manipulation of optical-pulse propagation, and concentration of electromagnetic energy for sensing applications. These features are all made possible by the strong mode confinement and short wavelengths of SPPs near their frequency limit as compared to guided or free-space electromagnetic waves.

2

The properties of SPPs are determined by their frequency-dependent complex wavevector. This may be calculated from the complex permittivity, which is empirically known for fourteen metals [1]. Numerous reports, from the most recent study [2] to the earliest [3], reveal significant unexplained discrepancies between theory and experiment. These are generally attributed, without analysis or any systematic proof, to surface morphologies, impurities, contamination, and lack of crystallinity for evaporated films. We here report initial investigations of surface plasmons generated in low-density nano-structured metal films, which opens a window to systematic study of SPPs on such films as a function of their microstructure. The nano-structure of gold-black affects the electron scattering frequency for currents excited by the SPP. This causes changes to the complex permittivity, which is detectable in the behavior of the SPP.

The real part of the complex wavevector for SPPs on metal films can be studied optically. SPPs are excited on the nano-structured metal films under conditions of total internal reflection for the optical beam within a prism. In this so-called Kretschmann method [4], the prism slows the optical beam so that, at the proper angle of incidence, the in-plane component of the optical wavevector matches wavevector of the surface plasmon at the photon frequency. At the surface Plasmon resonance angle, a sharp drop in the reflected optical power is observed. A standard X-ray goniometer was used to maintain the detector aligned with the reflected optical beam as the prism is rotated with respect to the incident beam. The source of light was a variety of lasers or a monochromated Xe arc lamp. The chopped reflected signal was detected by a photomultiplier or by a Si diode and synchronously lock-in amplified.

Surface plasmons will be excited on metal films deposited on dielectric prisms using a collimated monochromatic light source in the so-called Kretschmann configuration [4] shown in Fig. 2. In this experiment, the beam is incident on one of the small faces of a 90 degree prism and reflects internally from the large face at an angle that exceeds the critical angle. On the large face is deposited a film of metal of thickness such that some of the evanescent electromagnetic wave from the internally reflected optical beam penetrates to the outer surface. This thickness is of order 50 nm. When the component

of the wavevector of the optical beam parallel to the large prism surface equals the SPP
wavevector at the optical frequency, a SPP is generated. The intensity of the reflected
beam is monitored, and SPP generation is observed as a strong decrease in the
reflected optical intensity at the resonance angle.
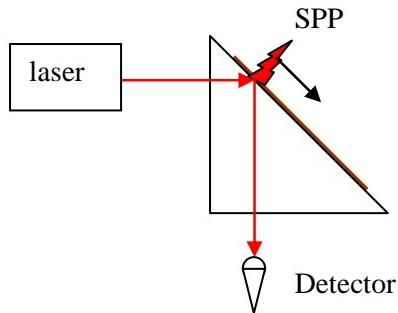
Fig. 2. Kretschmann configuration for generation of surface Plasmon polaritons and determination of
metal film permittivity.

Fig. 3 presents data collected at UCF for a nominally 50 nm thick smooth layer of pure
gold evaporated on a glass right-angle prism. The resonance positions are in
reasonable agreement with values calculated from published empirical permittivity data.
The resonance angle of incidence α_{res} is defined by

$$\text{Sin}[\alpha_{res}] = c\, k'/(\omega\, n), \tag{1}$$

where c is the speed of light, k′ is the real part of the SPP wavevector, and n is the
prism refractive index.
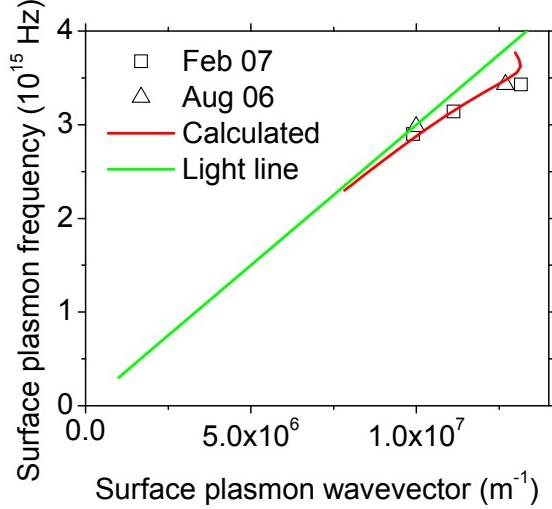
Fig. 3. (left) Surface Plasmon Polariton absorption resonances from Kretschmann experiment on smooth gold surface. (right) Surface Plasmon Polariton dispersion curve for smooth gold surface. The open squares are calculated values from published empirical complex permittivity. The solid symbols represent two sets of data collected by the Kreutchmann method at UCF using a Xe arc lamp and monochromator. The free space light line and the calculated dispersion curve for SPPs on gold.

The k' value is determined from the permittivity according to

$$k' = (\omega/c) \, \mathrm{Re}\{\sqrt{\varepsilon}/\sqrt{(1+\varepsilon)}\} \tag{2}$$

where

$$\varepsilon = \varepsilon' + i \, \varepsilon'' \tag{3}$$

is the complex permittivity. At 632 nm wavelength, we use ε = -11.6 + i 1.2 [5].

The effect of sample morphology is revealed by the change in the angular position of the SPP excitation peak and its line shape. The effect of the nanostructure of the gold is to broaden and shift the resonance peak. Fig. 4 presents a SPP resonance spectrum for a gold-black sample, and the line shape is clearly wider and the peak occurs at a larger angle than for corresponding optical frequency on smooth gold film (Fig. 3).

5
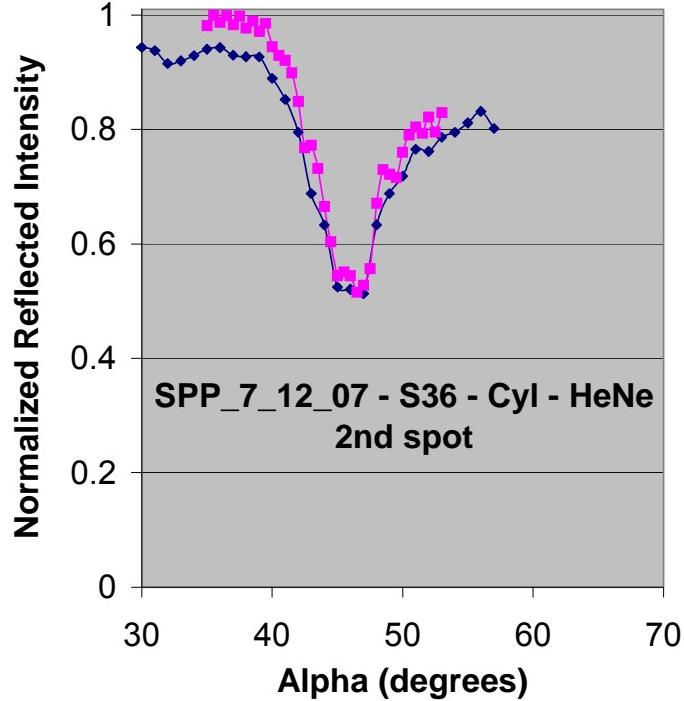
Fig. 4. Surface Plasmon resonance spectrum for gold-black film. The excitation was done using a HeNe laser at 632 nm wavelength.

The Fresnel equations for a three layer system allow one to extract the complex permittivity and thickness of the film from a fit to the resonance spectrum. For a metal film between two transparent dielectrics, the amplitude reflection coefficient is

$$r = (r_{12}\, e^{-2i\Psi} + r_{23}) / (e^{-2i\Psi} + r_{12}\, r_{23}) \qquad , \qquad (4)$$

where for a p-polarized incident beam

$$r_{12} = (\varepsilon_2\, k_{0z} - \varepsilon_1\, k_{2z}) / (\varepsilon_2\, k_{0z} + \varepsilon_1\, k_{2z}) \qquad (5)$$

and

$$r_{23} = (\varepsilon_3\, k_{2z} - \varepsilon_2\, k_{3z}) / (\varepsilon_3\, k_{2z} + \varepsilon_2\, k_{3z}) \qquad (6)$$

The change of phase over thickness h of layer 2 is

$$\Psi = (\omega/c)h\sqrt{(\varepsilon_2 - \varepsilon_1 \sin^2\theta_0)} \tag{7}$$

where θ_0 is the angle of incidence. In (2) and (3)

$$k_{0z} = (\omega/c) \sqrt{\varepsilon_1} \cos\theta_0 \tag{8}$$

$$k_{2z} = (\omega/c)\sqrt{(\varepsilon_2 - \varepsilon_1 \sin^2\theta_0)} = \Psi / h \tag{9}$$

$$k_{3z} = (\omega/c)\sqrt{(\varepsilon_3 - \varepsilon_1 \sin^2\theta_0)} \tag{10}$$

Because the metal permittivity $\varepsilon_2 = \varepsilon_2' + i\,\varepsilon_2''$ is complex, k_{2z} and Ψ are complex, and consequently so are r_{12}, r_{23}, and r. The reflection coefficient is R = rr*, which can be plotted as a function of θ_0. In our Kretschmann experiment, medium 1 is glass, medium 2 is solid metal or gold black, and medium 3 is air.

In s-polarization, the only changes are to Eqs. (5) and (6), which become

$$r_{12} = (k_{0z} - k_{2z}) / (k_{0z} + k_{2z}) \tag{11}$$

and

$$r_{23} = (k_{2z} - k_{3z}) / (k_{2z} + k_{3z}) \quad . \tag{12}$$

A Mathematica program, given next, was written to calculate the reflectance R vs angle of incidence.

```
(*Peale018.  Program to calculate 3-layer Fresnel reflection.
prism/gold/air*)
(*fundamental constants*)
c=2.997925 10^8  (*speed of light, m/s*);
```

7

```
p=Pi//N;
(*materials constants*)
e1=1.48 ^2 (*real permittivity of prism*);
e2=-11.6 + I 1.2 (*complex permittivity of gold at 632 nm, JC value
from Raether*);
e3=1 (*permittivity of air*);
d=50 10^-9 (*gold thickness, m*);
(*equations*)
k0z[q_]:=2 p/(632 10^-9) Sqrt[e1] Cos[q];
k2z[q_]:=2 p/(632 10^-9) Sqrt[e2-e1 Sin[q]^2];
k3z[q_]:=2 p/(632 10^-9)Sqrt[e3-e1 Sin[q]^2];
psi[q_]:=k2z[q] d;
r12[q_]:= (e2 k0z[q] - e1 k2z[q]) / (e2 k0z[q] + e1 k2z[q]);
r23[q_]:= (e3 k2z[q] - e2 k3z[q]) / (e3 k2z[q] + e2 k3z[q]);
r[q_]:=(r12[q] Exp[-2I psi[q]] + r23[q]) / (Exp[-2I psi[q]]+ r12[q]
r23[q]);
Plot[Abs[r[q]]^2,{q,0,p/2}, PlotRange->{0,1}]
t1 = Table[{180 q/p, Abs[r[q]]^2}, {q, 0, p/2, 0.001}]
```

Fig. 5 presents calculated reflectance spectra for nominal material characteristics. The SPP resonance is seen in p-polarization only, and only when the incident medium has index greater than unity. The resonance occurs only at angles of incidence greater than that for total internal reflection within the prism material. Comparison of the calculation to data for 632 nm excitation shows angular-position and depth discrepancies for the resonance that can be attributed to the uncertainty in the prism index and film thickness.
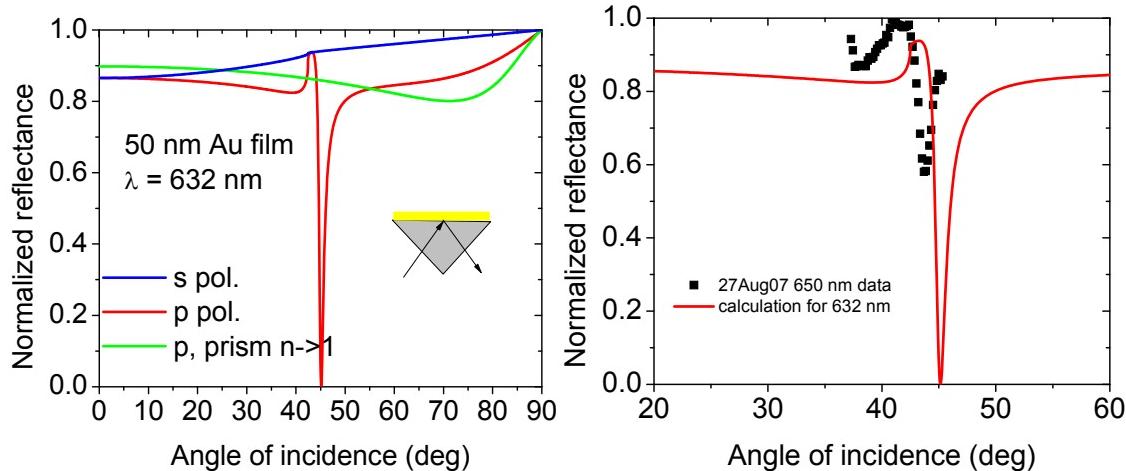

Fig. 5. (left) Calculated reflectivity spectra. (right) Comparison of calculation with collected data for nominal film thickness, prism index, and published gold permittivity values.

Fig. 6 presents calculations for incidence from the air side. These results further confirm that a resonance occurs only when the incident medium has a refractive index

that exceeds that of the medium on the far side of the film. Also the prism is found to have only a small effect on the reflectance curve for p-polarization, in contrast to what is found for incidence from the prism side.
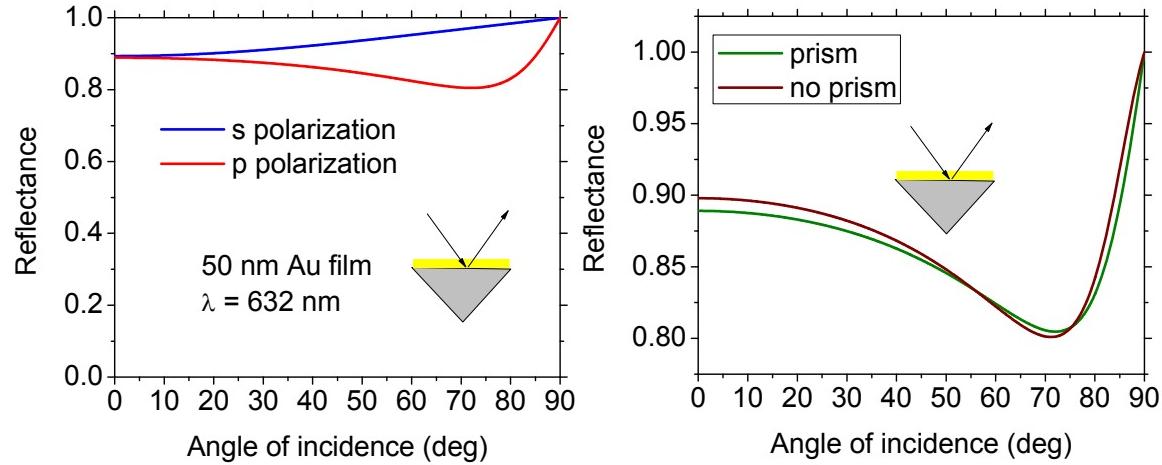
Fig. 6. Calculated reflectance curves for incidence from the air side.

The Mathematica program below gives a routine for fitting the Fresnel formula to the reflectance data.

```
(*Peale020.  Program to fit 3-layer Fresnel formula, p polarization,
prism/gold/air, to Kreutschman data*)
(*Get data from thumb drive*)
SetDirectory["E:"] ;
t1=Import["SP27AG07rad.dat","CSV"];
(*fundamental constants*)
c=2.997925 10^8  (*speed of light, m/s*);
p=Pi//N;
(*materials constants*)
e2=-11.6 + I 1.2 (*complex permittivity of gold at 632 nm, JC value from
Raether*);
e3=1^2 (*permittivity of air*);
(*equations*)
k0z[q_]:=2 p/(632 10^-9) Sqrt[e1] Cos[q];
k2z[q_]:=2 p/(632 10^-9) Sqrt[e2-e1 Sin[q]^2];
k3z[q_]:=2 p/(632 10^-9)Sqrt[e3-e1 Sin[q]^2];
psi[q_]:=k2z[q] d;
r12[q_]:= (e2 k0z[q] - e1 k2z[q]) / (e2 k0z[q] + e1 k2z[q]);
r23[q_]:= (e3 k2z[q] - e2 k3z[q]) / (e3 k2z[q] + e2 k3z[q]);
r[q_]:=(r12[q] Exp[-2I psi[q]] + r23[q]) / (Exp[-2I psi[q]]+ r12[q] r23[q]);
bigR[q_]:=Abs[r[q]]^2;
FindFit[t1,bigR[q],{{e1,2.25},{d,50 10^-9}},q]
```

Fig. 7 presents the result of the fit together with the data. In this fit, the solid gold permittivity was considered to be known, and the film thickness and prism index were

9

considered as fitting parameters. The fitting parameters given in the plot are in reasonable agreement with the nominal values. Only trivial modification of the fitting routine is required to find ε_2', ε_2'', and the film thickness h for gold black.
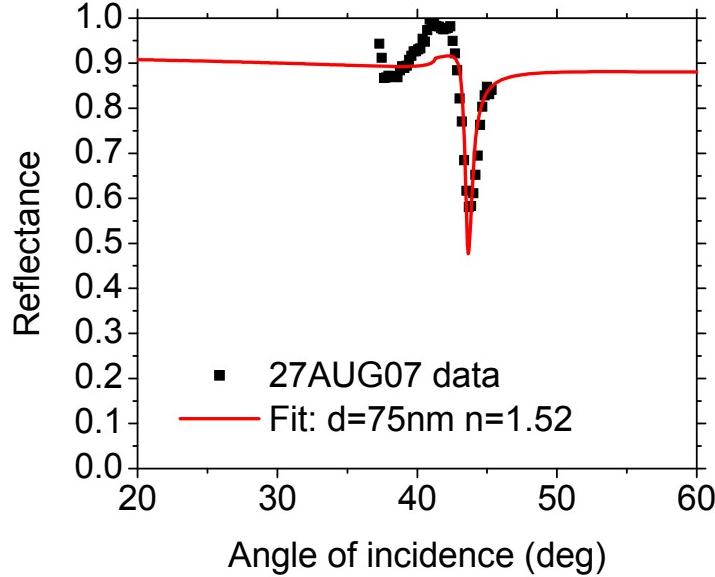
Fig. 7. Fit of Fresnel formula to reflectance data for gold.

2.3 Electron Beam Measurements

As the SPP frequency increases, their propagation lengths decrease rapidly to values of a few hundred nanometers. SPP propagation over such distances may be detected by cathodoluminescence as demonstrated recently by van Wijngaarden et al. [6]. This technique was explored at UCF using a Philips XL30 SEM integrated with a Gatan MonoCL3 system for high-resolution cathodoluminescence imaging and spectroscopy. A photograph of the SEM-CL setup is presented in Fig. 8. The cathodoluminescence system is equipped with a high efficiency collector consisting of a parabolic mirror and light guide (**2**, Fig. 8), which is directly coupled to the integrated monochromator (**3**, Fig. 8). Photons out-coupled by the grating from the SPPs, which are generated by the electron beam, are immediately directed onto the entrance slit of the chamber-mounted monochromator, avoiding any losses associated with conventional optical fiber coupling. Thus, spectral analysis or monochromatic imaging can be carried out with a spectral resolution of up to 0.5 nm. As standard, MonoCL3 is fitted with a photo-multiplier (**4**, Fig.

8), sensitive in the 200-850 nm range, and a 1200 lines/mm grating. This configuration allows a serially-scanned data collection over the specified range. Steps and dwell time per point determine the length of the acquisition time.
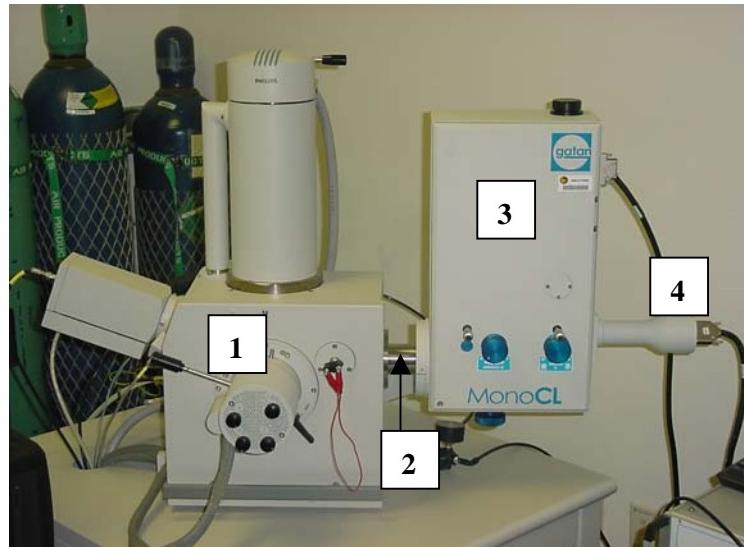
Fig. 8. SEM-CL setup. 1 –SEM vacuum chamber; 2 – Light guide; 3 –Monochromator; 4 – PMT

A 471 nm thick Gold layer was e-beam evaporated on a 5 nm Cr sticking layer on a polished silicon wafer substrate. Several 20 period gratings were cut in the gold layer using a 30 keV focused gallium-ion beam (FIB). The nominal period was 600 nm and the widths of the grooves were varied. Fig. 9 presents an FIB image of one of the gratings prepared. This grating has 120 nm groove widths. Fig. 9 indicates schematically the e-beam spot at a distance x from the grating. The e-beam spot is in reality only a few nm across, i.e. at least 100 times smaller than its representation in Fig. 9. Imaging the finished grating with a 100 pA gallium beam ablates the gold surface in a large square region surrounding the cut gratings, and this affects the background CL emission spectrum, as will be shown below.
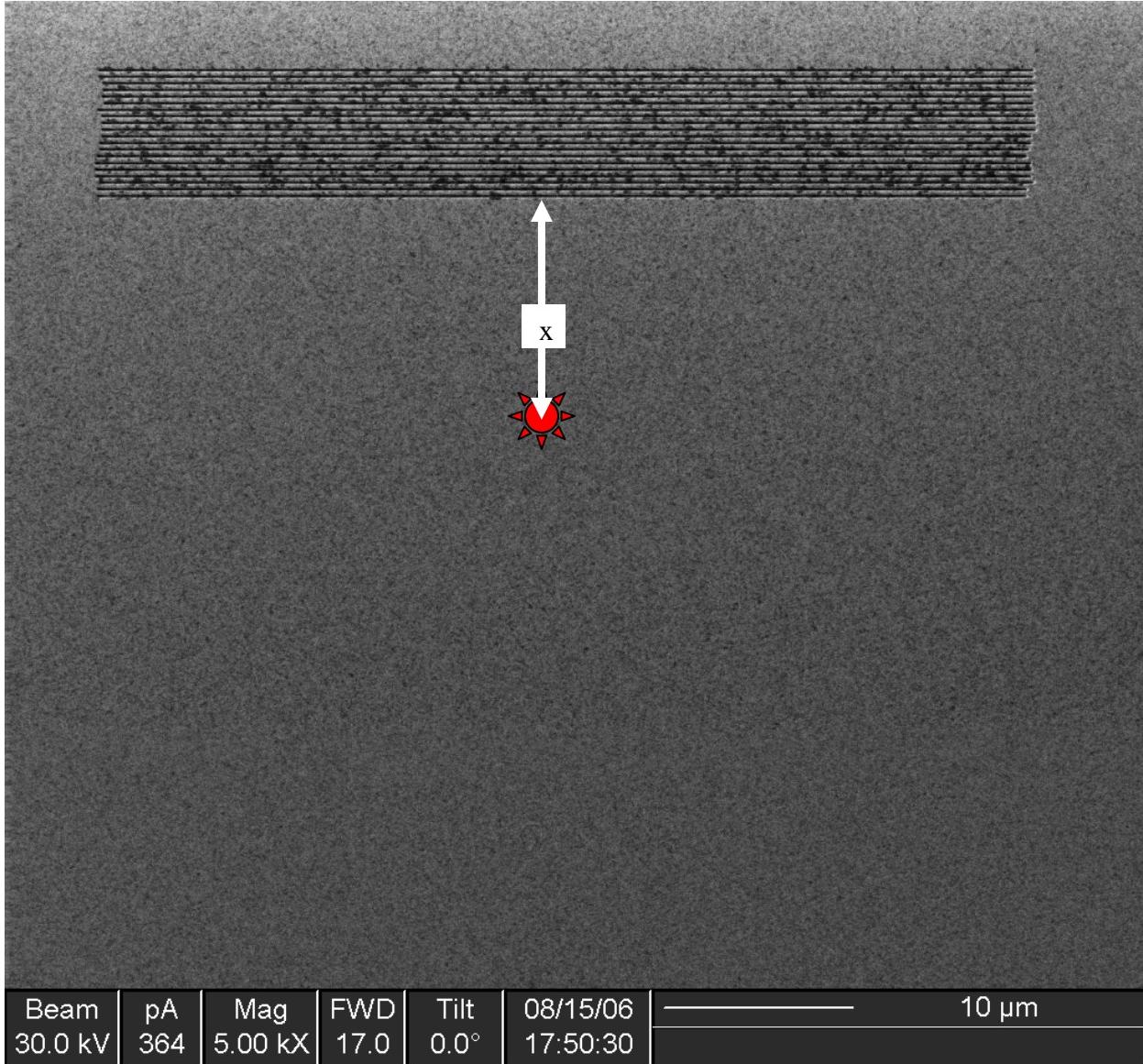
Beam	pA	Mag	FWD	Tilt	08/15/06	10 µm
30.0 kV	364	5.00 kX	17.0	0.0°	17:50:30	

Fig. 9. FIB image of grating cut in gold on silicon substrate. The red star is a schematic representation of the few nm diameter electron beam spot (exaggerated for clarity) at a distance x from the rulings. A cathodoluminescence spectrum is collected a various values of x.

The measurement of SPP propagation lengths works as follows. The focused electron beam is incident on the metal film and excites surface plasmons of all frequencies below the SPP limit. The SPP excitation probability is sharply peaked at the surface Plasmon resonance frequency $\omega = \omega_p/\sqrt{2}$ for Drude metals [7]. For gold, a non-Drude metal in the visible, the distribution should still peak somewhere at high visible frequencies. The surface plasmons propagate along the surface in all directions. Those that encounter the grating are coupled into free electromagnetic waves which are collected into the monochromator and detected by the photomultiplier tube. By varying

the distance between the electron beam and the grating, one can determine the characteristic SPP propagation length L at each wavelength setting of the monochromator from a plot of collected intensity vs. distance. Our experiments were performed by holding the distance constant while collecting the entire CL spectrum.

The SPP propagation length L is the inverse of the frequency-dependent imaginary part k′′ of the SPP wavevector given by

$$L^{-1} = k'' = (\omega/c)\, \text{Im}\{\sqrt{\varepsilon}/\sqrt{(1+\varepsilon)}\} \qquad . \tag{13}$$

Fig. 10 presents the calculation SPP propagation length as a function of the optical wavelength that corresponds to the SPP frequency. Empirical permittivity values for gold used in Eq. (13) were taken from [5]. Note that the propagation is always less than 100 μm in the visible spectral range. Also indicated in Fig. 10 is the range of optical wavelength collected and the range of distances x of the e-beam from the grating in the CL experiment.
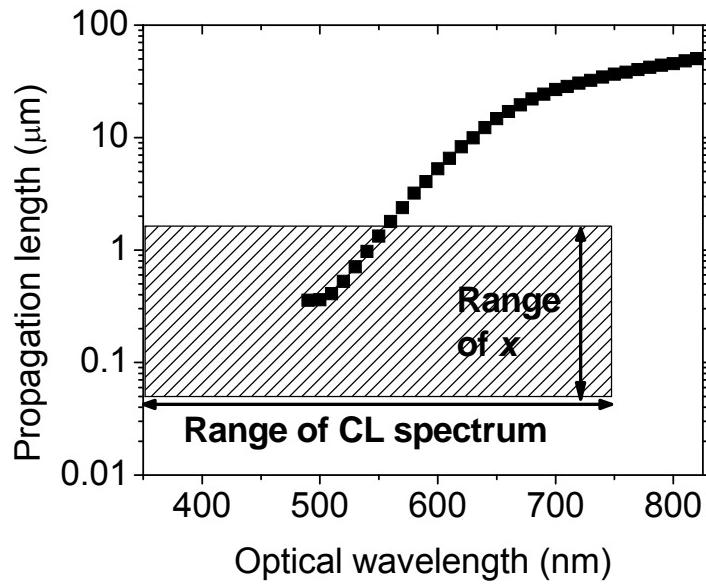
Fig. 10. Calculated SPP propagation length on gold.

Fig. 11 presents ratios of cathodoluminescence (CL) spectra. In these spectra the numerator is a spectrum taken near the grid and the denominator is a reference spectrum taken at a distance much larger than the anticipated SPP propagation length at any of the optical frequencies considered (Fig. 10). Thus the denominator spectrum corresponds to pure background CL, while the numerator can contain contributions from surface plasmons that are out-coupled by the grating.

That the ratios in Fig. 11 are nearly everywhere somewhat less than unity indicates that the background CL is slightly stronger far from the grating. This can be explained by the cleaning of the surface near the grating that occurred during FIB imaging of the cut grating. The imaging spot extends out to of order 50 μm from the grating (Fig. 9). Due to imperfect focusing of the Ga beam, and the extra time spent by the gallium beam close to the grating while it was being cut, one might expect that the background CL would increase gradually as distance x of the e-beam from the grooves increased. This can explain the rise in the ratio toward unity as the e-beam is moved farther from the grating in Fig. 11 (right).
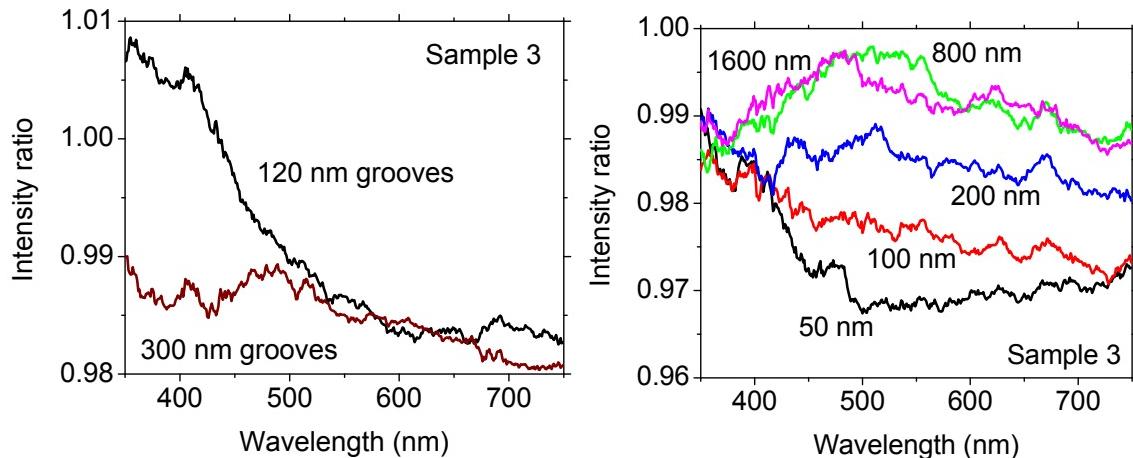

Fig. 11. (left) Ratio of cathodoluminescence spectrum collected at 1 micron and 100 micron distance from the 600 nm period 20 line grating, for two groove widths. (right) . Ratios of CL spectra collected at the indicated distances from the grating to a CL spectrum collected 1 mm from the grating.

In comparison to the paper by van Wijngaarden et al., our background signal is much stronger than any signal due to SPPs outcoupled by the grating. To estimate whether this background can be attributed to outcoupling by surface roughness, we performed AFM measurements on similarly evaporated gold films. Fig. 12 presents an AFM image of a particularly rough sample. One observes small islands of gold of approximately 50 nm lateral dimension and about 4 nm height. On all other samples studied, the size of the islands was smaller than 50 nm.
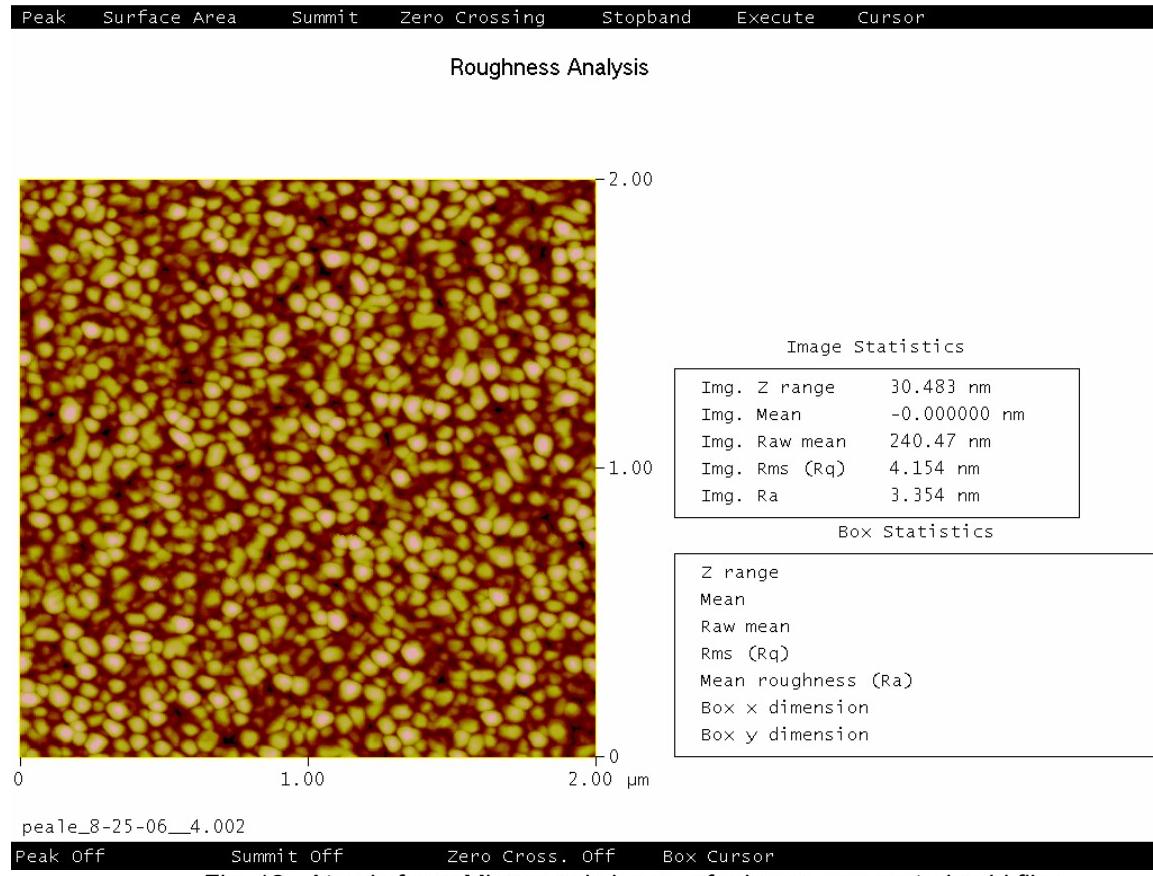
Fig. 12. Atomic force Microscopic image of e-beam evaporated gold film.

To determine if such roughness would efficiently outcouple surface plasmons, we suppose that the surface represents a grating with period a = 50 nm. Then the relation between the surface Plasmon wavevector k' and the angle θ for emission of light due to coupling between the SPP and the "grating" is

$$k' = (2\pi/\lambda) \sin\theta + 2\pi \, m/a, \qquad (14)$$

where m is an integer including negative values and zero. Numerical values of k' for each value of λ are calculated from

15

$$k' = (\omega/c)\ \mathrm{Re}\{\sqrt{\varepsilon}/\sqrt{(1+\varepsilon)}\} \qquad . \qquad\qquad . \ (15)$$

Fig. 13 plots k' as a function of the optical wavelength corresponding to surface plasmons of frequency ω. Except at the shortest wavelength, θ has no solution for any integer *m*. At the shortest wavelength, the value of θ is close to 90 degrees, so that such emission would not be collected by the CL setup. We conclude that *none* of the large background emission arises from generation and outcoupling of SPPs into free space EM waves. For comparison, the same analysis applied to the cut 600 nm grating predicts a solution (for *m*=1) giving an outcoupling angle for SPP emission into free space waves of ~11 deg in the range 490-750 nm. Such an emission is very likely collected by the CL apparatus, and the collection efficiency would be a very weak function of wavelength.
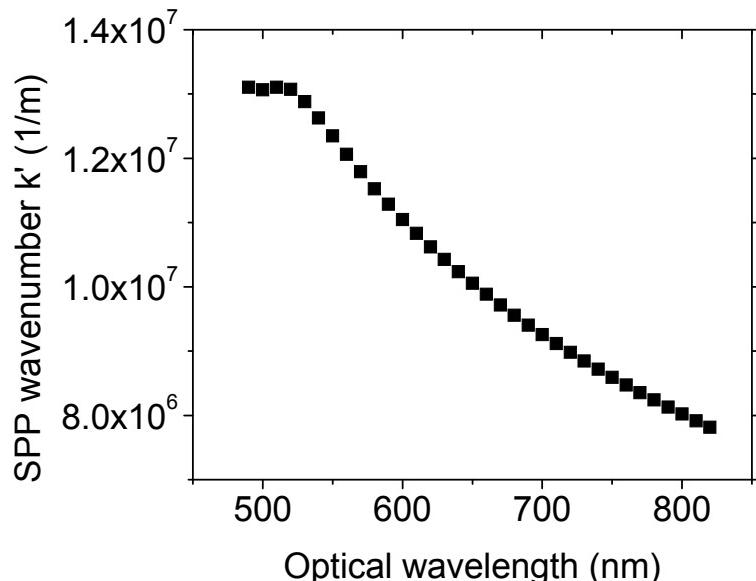

Fig. 13. Calculated real part of the SPP wavevector for gold as a function of the optical wavelength that corresponds to the SPP frequency.

The emission spectrum I(x,λ) with position dependent background spectrum may be taken to have the form

$$I(x,\lambda) = B(\lambda)\, f(x) + p(\lambda)\, \mathrm{Exp}[-x/L(\lambda)], \qquad\qquad (16)$$

where the background spectrum $B(\lambda)$ is that measured far from the grating (x>>L) on regions of the as-deposited film that were untouched by the gallium beam of the FIB. Assuming that the gallium beam cleans the surface and reduces the background, the factor f(x) must be everywhere $\leq$ 1, becoming smaller as the e-beam approaches the grating. The function $p(\lambda)$ represents the distribution of surface plasmons at the frequency ω excited by the electron beam, together with the probability of their being outcoupled by the grating, the probability of being collected by the spectrometer, and the spectrometer's spectral response function. The latter probabilities are expected to be weak functions of λ in comparison to the probability of surface Plasmon generation. From Ref. [7] we expect that the probability of generation is sharply peaked at $\omega_p/\sqrt{2}$ (for an ideal metal), and for our case of gold and a spectrometer with short wave cutoff at 350 nm, we may simply assume that $p(\lambda)$ decays rapidly with increasing λ.

The ratio of CL spectra, such as plotted in Fig. 11, is given by

$$R(x,\lambda) \equiv I(x,\lambda)/I(x>>L,\lambda) = f(x) + r(\lambda) \, Exp[-x/L(\lambda)], \qquad (17)$$

where $r(\lambda) = p(\lambda)/B(\lambda)$ is assumed to be dominated by the sharply decay in $p(\lambda)$ with wavelength. Setting f(x) = 1 for all x, taking $r(\lambda)$ to be an exponential decreasing function of λ, and using calculated $L(\lambda)$ values (Fig. 10), we generate the family of curves plotted in Fig. 14. These are qualitatively similar to the experimental curves in Fig. 10, in that the 50 nm curve is peaked at the shortest wavelength while the curves for longer wavelength have a hump in their middle. The comparison will be closer if f(x) is taken <1 and allowed to decrease as x decreases. The spectral shape of the calculated spectra can be made closer to the measured curves by adjusting the function $r(\lambda)$.   The main point to be made here is that the observed curves in Fig. 11 make sense in terms of the physics and likely experimental factors.

1+0.1*Exp[-λ/100 nm]*Exp[-x/L(λ)]
50 nm
100 nm
200 nm
800 nm
1600 nm
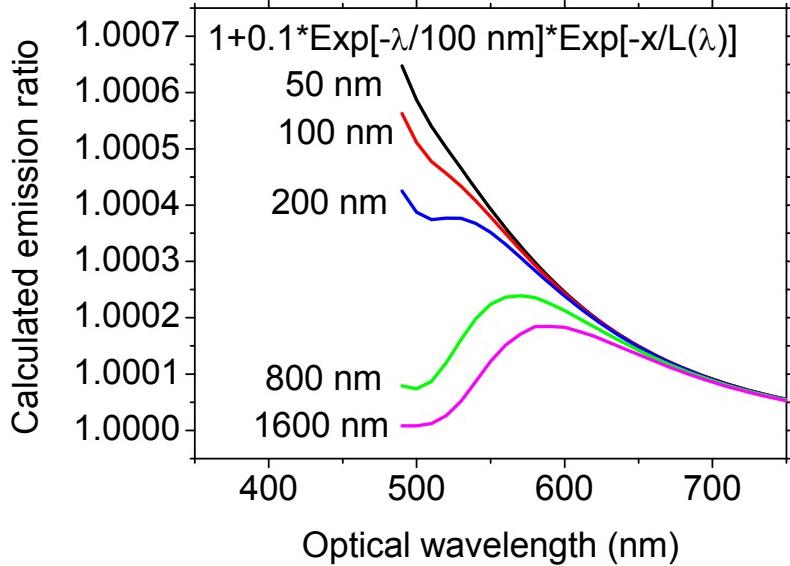
Fig. 14. Simulated CL intensity ratios.

3. TWO DIMENSIONAL PLASMONS IN InP-BASED HEMT

Plasmons can be generated with photons in the two dimensional electron gas (2-deg) of high electron mobility transistors (HEMTs). Because the plasmon frequency at a given wavevector depends on sheet charge density, a gate bias can tune the plasmon resonance. This effect allows a properly designed HEMT to be used as a voltage-tunable narrow-band detector or filter. This part of the report describes both the theory and design of such a device in the InP materials system and discusses its potential uses. By using a sub-micron grating to couple incident radiation to a high sheet charge 2-deg, a minimum detectible wavelength of roughly 26 μm is obtained. Fabrication issues, terahertz response, and tunability are discussed. Because of its small size, this novel device could find use in spaceborne remote sensing application.

Plasmons are charge density oscillations whose generation in semiconductor heterostructures provides a mechanism for tunable wavelength-selective detection at terahertz frequencies. This class of frequency agile detector holds promise for the development of a true spectrometer-on-a-chip for chemical and biological detection due to the rich spectra found at these frequencies. Two-dimensional plasmon resonances observed in Si MOSFETs [8] and AlGaAs-based semiconductor heterostructures [9,10]

18

tune with 2-deg sheet charge density, which is controlled by a gate bias. Surprisingly, a change in device conductivity has also been found to accompany the plasmon resonance of such devices. This has led to research concerning the use of high electron mobility transistors (HEMT's) as frequency agile, voltage tunable detectors. In effect, incident THz radiation excites a bias-controlled plasmon resonance, which is observed as a change in the device transconductance. This work explores a device design based on the InP materials system, which is new. We report on maximum achievable resonance frequency, tuning range, resonance linewidth, temperature effects, incident radiation coupling considerations, and device fabrication.

The dispersion relationship for a plasmon in a 2-deg is [8]

$$\omega_p(k_p) = \sqrt{\frac{n_s q^2 k_p}{m^* \varepsilon_o (\varepsilon_b + \varepsilon_t Coth(k_p d))}} \quad , \tag{18}$$

where all quantities are expressed in S.I. units, ω_p is the plasmon frequency, k_p is the plasmon wave vector, q is the elementary charge, m^* is the electron effective mass in the 2-deg, d is the distance of the 2-deg below the semiconductor surface, ε_b and ε_t are the relative dielectric constants of the material below and above the 2-deg respectively, ε_0 is the permittivity of free space, and n_s is the 2-deg sheet charge density. Eq. (18) shows that for any incident photon with wave vector $k_i (= \frac{\omega_i}{c})$ and any angle of incidence, photon momentum is insufficient to excite a plasmon, i.e for $\omega_i = \omega_p, k_{i\|} < k_p$ always. To conserve momentum and excite a plasmon, additional in-plane photon momentum can be acquired from a grating on the semiconductor surface. For normal incidence, the acquired parallel component of the wavevector is

$$G_m = 2 \pi m/a , \tag{19}$$

where a is the grating period, and m is an integer ($m= \pm 1,2,\ldots$). Thus, for radiation at normal incidence to a properly designed grating, both energy and momentum can be conserved in the generation of a plasmon with $G_m = k_p$. The grating (possibly enhanced by an underlying semitransparent metallic layer) can also serve as the transistor gate to

permit bias-control of the 2-deg sheet charge density (n_s) and tuning of the resonance frequency, thereby creating a spectrometer-on-a-chip.

The detection range of this type of detector is determined by the sheet charge density, electron effective mass in the 2-deg, and the grating period. Because larger grating periods are easier to fabricate, and because lower sheet charge densities are easier to obtain, this type of device is best suited to long wavelengths. A goal of this work is to seek shorter wavelength response than has been achieved previously. The epitaxial layer structure presented schematically in Fig. 15 is chosen because similar InGaAs/InAlAs/InP structures have demonstrated high sheet charge densities [11,12].

Eqs. (18) and (19) determine the high frequency limit of the Fig. 15 structure. Required material parameters are found as follows. The permittivity of semiconductor alloy $A_{1-x}B_x$ is determined from the permittivities ε_A, ε_B of the end members A,B according to

$$\varepsilon_{AB} = (1-x)\varepsilon_A + x\varepsilon_B - x(1-x) \ , \tag{20}$$

for both InGaAs and InAlAs [13]. Using ε_{AlAs}=10.2, ε_{InAs}=14.6, and ε_{GaAs}=13.1, we obtain ε_i=12.2 for the $In_{0.52}Al_{0.48}As$ layer above the 2-deg and ε_b=13.9 for the $In_{0.68}Ga_{0.32}As$ below the 2-deg. Using an effective mass of 0.043 for electrons in the InGaAs channel [14], we obtain from Eq. (15) a plot (Fig. 16) of excitation frequency versus sheet charge density and grating period. From Fig. 16, a grating period of 0.1 μm and a sheet charge density of 3 x 10^{12} cm^{-2} provide a minimum detectible wavelength of 26 μm.

| 75A $In_{0.60}Ga_{0.40}As$ 6x10^{18} cm^{-3} Cap |
| :---: |
| 350A $In_{0.52}Al_{0.48}As$ Buffer Undoped |
| 4x10^{12} cm^{-2} Si δ doping |
| 30A $In_{0.52}Al_{0.48}As$ Set Back Undoped |
| 200A $In_{0.68}Ga_{0.32}As$ Channel |
| 30A $In_{0.52}Al_{0.48}As$ Set Back Undoped |
| 4x10^{12} cm^{-2} Si δ doping |
| 3000A $In_{0.52}Al_{0.48}As$ Buffer Undoped |
| Semi-insulating InP substrate |
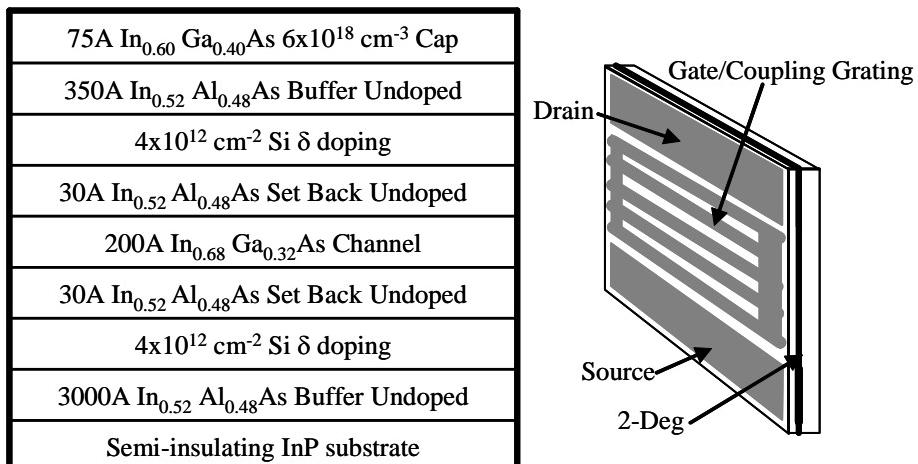
Fig. 25. Epi-layer structure and device schematic used for the voltage tunable plasmon based detector of this work

To determine the effects of gate bias, the 2-deg sheet charge density, n_s, is given by

$$n_s = C_{gate} \frac{(V_g - V_t)}{qLW} , \qquad (21)$$

where V_g is the gate bias, V_t is the device threshold voltage, L is the gate source to drain spacing, W is the gate width and C_{gate} is the gate capacitance. The latter can be approximated (in S.I. units) by

$$C_{gate} = \frac{\varepsilon_t \varepsilon_o LW}{d} . \qquad (22)$$
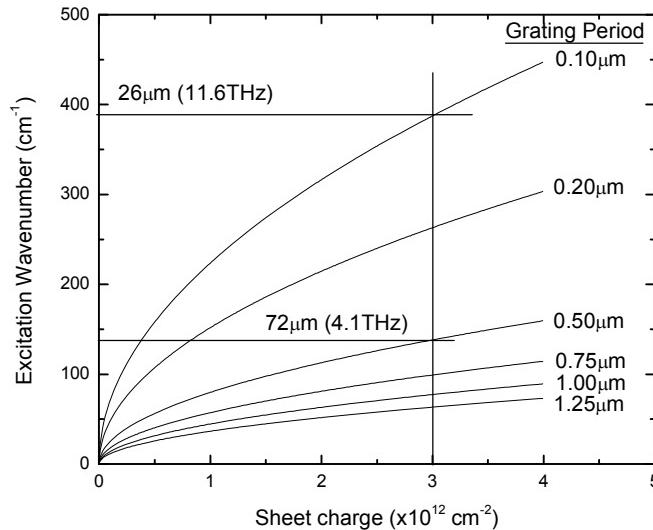

Fig. 16. Incident excitation wave number as a function of 2-deg sheet charge density for various grating periods.

The threshold voltage, V_t, is given by

$$V_t = \phi_b - E_c - \frac{q n_d d}{\varepsilon_t} , \qquad (23)$$

where n_d is the delta doping concentration of the heterostructure and E_c is the conduction band offset. For the InGaAs/InAlAs system, when the In mole fraction in $In_x Ga_{1-x} As$ exceeds 58%, E_c is given by [15]

$$E_c = 0.344 + 0.487x . \qquad (24)$$

21

For an MBE grown epi-layer structure of Fig. 15 design, Hall measurements indicate a sheet charge density of 2.4 x 10^{12} cm^{-2} and a mobility of 10100 (26500) cm^2/V-s at 300 (77) K. Using a typical barrier height for metal on a III-V compound of ϕ_b = 0.7 eV and all other values as previously defined, a linear decrease in sheet charge is expected with a maximum value at V_g=0 and zero at V_g=-1.3 V.

Fig. 17 presents the physical layout of the device studied theoretically in this work and to be explored experimentally in the near future. The overall chip size is 3.5 mm x 3.5 mm with the gate/grating measuring 250 μm x 195 μm. Care was taken to overlap all of the various metallization layers so that light can only be transmitted through the central gate/grating region of the device. The gate/grating section of this device is fabricated by first depositing a semitransparent Ti layer (with a sheet resistance assumed for calculation purposes to be $\rho_h \sim 350\Omega/sq.$) On top of this will be deposited Au grating stripes (with a sheet resistance assumed for calculations to be $\rho_l \sim 0.14\Omega/sq.$) Initial measurements on this device will be made using a high-power THz p-Ge laser at liquid helium temperatures. A multimode output spectrum presented in Fig. 18a demonstrates its suitable bandwidth[16] and a range of features that can be recorded as the device resonance tunes with gate bias. The device of Fig. 17 is mounted in the He dewar between the p-Ge laser and a Ge:Ga photodetector as shown in Figure 18b. Electrical leads connecting source, drain and the gate/grating are then used to vary the sheet charge density while monitoring the device transconductance. Transmission through the device can be simultaneously monitored with the 4 K Ge:Ga photoconductor. Based on the spectrum for the p-Ge laser and the maximum measured sheet charge of the epilayers, a grating period of 0.5 μm has been chosen to allow tunable detection across the entire output bandwidth of the laser with gate voltages from 0 V to -0.6 V.
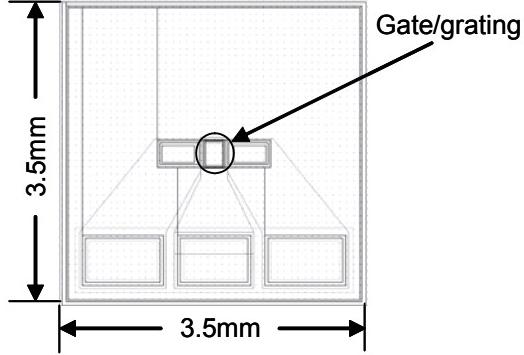
Fig. 17. Physical layout of device used in this work. Overlapping metal ensures light only passes through central gating/gate for maximum dynamic range during transmission measurements.
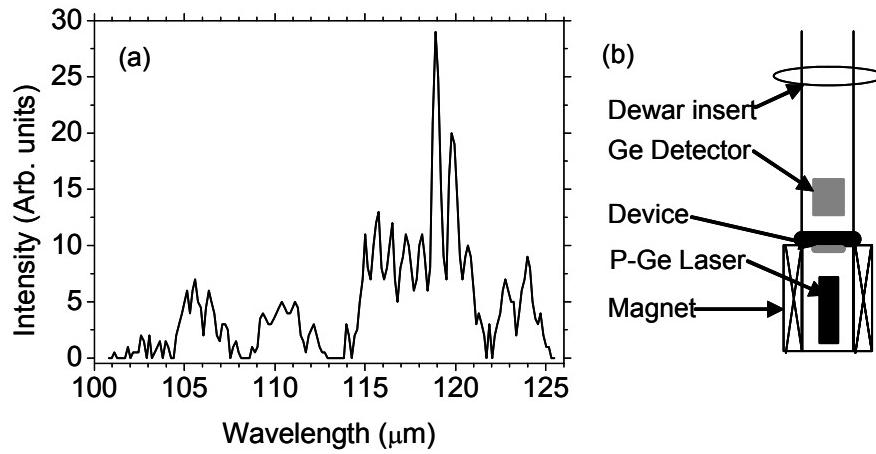

Fig. 18. (a) Typical output spectra of p-Ge laser used to excite plasmon resonance and (b) Schematic of transmission and photoconductivity experiment.

To determine the features of the Plasmon resonance spectra in more detail, the theory of plasmons in grating-coupled 2-deg devices is used here [17]. Referring to Fig. 19, spatially uniform THz electric fields polarize the grating bars, which induces local fringing fields with the grating periodicity. These *x-y* polarized local fringing fields excite the plasmons in the 2-deg. The transmittance, *T*, of un-polarized light is

$$T = (T_y + T_z)/2 \ , \tag{25}$$

where T_y in zero magnetic field and in Gaussian units is

$$T_y = \sqrt{\varepsilon_b} \left| \frac{2}{1 + \sqrt{\varepsilon_b} + \Sigma_{yy} \frac{4\pi}{c}} \right|^2 \ , \tag{26}$$

and T_z is obtained by substituting *z* for the *y* subscript. The complex *yy*-component of the conductivity tensor is

$$\Sigma_{yy} = \sigma(\omega) + \sigma_{yy}^g \ , \tag{27}$$

while the *zz*-component is given by

$$\Sigma_{zz} = \sigma(\omega) + <\sigma_{zz}^g> \ , \tag{28}$$

where < > indicates a spatial average, and $\sigma(\omega)$ is the conductivity associated with the 2-deg only. The second terms are components of the grating conductivity tensor. Only σ_{yy}^g interacts with the 2-deg. The $<\sigma_{zz}^g>$ is independent of the 2-deg because of the lack of fringing field components polarized in the z-direction. All off-diagonal components of Σ vanish in the absence of a magnetic field.
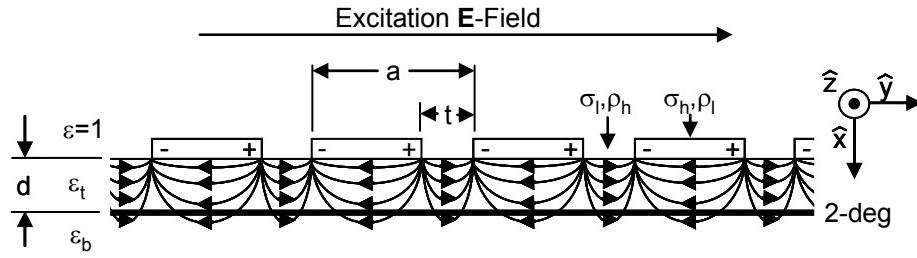

Fig. 19. Illustration of effects of incident excitation field on grating and in-turn on the 2-deg for this device.

The frequency dependent conductivity of the 2-deg is

$$\sigma(\omega) = \frac{n_s q^2 \tau}{m^*(1 + \omega^2 \tau^2)} \ , \tag{29}$$

where τ ($= \frac{m^* \mu}{q}$) is the electron relaxation time and μ is the temperature-dependant electron mobility. The last term of Eq. (27) is treated in the perturbative approximation according to

$$\sigma_{yy}^g = \frac{1}{<\rho>} - \sum_{m>0} \left(\frac{\tilde{\rho}(m)}{<\rho>} \right)^2 \frac{F_m}{2} \ , \tag{30}$$

where $<\rho>$ is the spatially averaged 2D resistivity of the grating, $\tilde{\rho}(m)$ is the mth Fourier coefficient in the Cosine expansion of the *yy*-component for the grating resistivity tensor given by

$$\tilde{\rho}(m)=\frac{2}{\pi m}(\rho_h-\rho_l)Sin\frac{\pi t m}{a} \quad , \tag{31}$$

and

$$F_m=(i\,\omega/4\pi G_m)\left[1+\varepsilon_t Coth(G_m d)+\frac{\varepsilon_b^2(1-Coth^2(G_m d))}{\frac{4\pi i}{\omega}G_m\sigma(\omega)+\varepsilon_b+\varepsilon_t Coth(G_m d)}\right]. \tag{32}$$

Following Ref. 17, the sum Eq. (30) is truncated after m = 10.

For the Fig. 15-based as-grown MBE structure, electron relaxation times of τ= 0.25 (0.65) ps were measured at 300 (77) K. As will be shown below, these values are insufficiently high to produce sharp plasmon resonances, but they can be increased by cooling the device. Fig. 20 plots τ vs T, where the measured data points appear as symbols. Assuming that phonon scattering dominates the carrier relaxation, the temperature dependence should obey a power law with a -3/2 exponent [18], which we use to estimate the low temperature τ values even though the actual data fall on a curve with an exponent closer to -0.70 (light line).
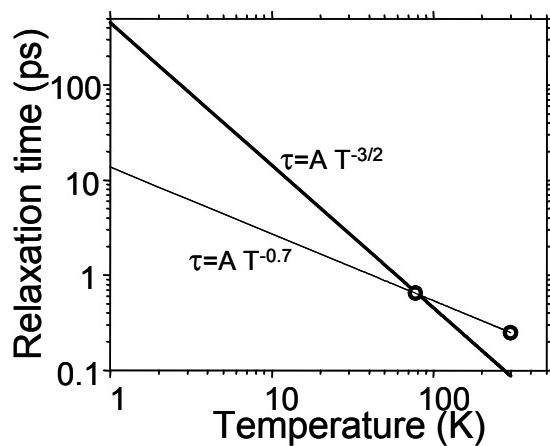

Fig. 20. Temperature dependence of the relaxation times for the 2-deg of this work. Symbols represent values calculated from the measured mobility. The $T^{-3/2}$ curve (heavy line) is a least squares fit to the data and was used for all simulations, although the $T^{-0.7}$ curve (light line) represents a better fit to the limited data.

Based on the theory and design presented above, transmission spectra are calculated, assuming a grating period a = 0.5 μm and a 2-deg depth d = 37 nm. Fig. 21 illustrates the effects of sheet charge and effective mass uncertainty at 4 K, where the sheet charge density of 2.4 x 10^{12} cm^{-1} is varied by a factor of two, while the effective mass of 0.043 is increased by 50% to 0.065 [19]. With these changes in material parameters no change is seen in the plasmon FWHM of ~1.7 cm^{-1}. Changing the effective mass by 50% however causes a 19% decrease in the peak position wave number. Changing only the sheet change by a factor of two causes a 29% decrease in the peak position wave number. Uncertainty in peak position of this magnitude does not affect our planned experiment with the p-Ge laser, whose full tuning range is 50-140 cm^{-1}. It is noted, that although the peak position accompanying these material changes could be determined by the much simpler Eq. (1), the more detailed theory of Ref [10] is required to determine the overall plasmon line shape.

Resonance line width and absorption strength depend on temperature as shown in Fig. 22 (a) and (b). Fig. 22 (a) shows typical 1st order transmittance spectra for n_s = 2.4 x 10^{12} cm^{-2} and t/a = 0.65. The temperature dependence of metallization resisitivity is ignored because resistivity changes in the semi-transparent gate affect mainly the baseline transmittance. Moreover, residual resistance for thin semitransparent Ti films can be so high that the temperature is weak [20]. The thick Au grating bars are opaque and the decrease in their resistivity with cooling has no effect on the spectrum at all. Fig. 22 (a) shows that there is still a small but measurable signal even at a temperature of 100 K. Fig. 22 (b) plots both the percentage change of the transmittance as well as the simulated full width half maximum (FWHM) of the resonance peak for both 1st and 2nd order resonances. It is clear from this plot that the 2nd order peaks are not as deep and are slightly narrower in line width at lower temperatures.

Fig. 23 presents the transmission plotted as a function of t/a ratio for both the 1st and 2nd order resonances. Fig. 23 (a) shows similar peak heights for all t/a ratios with a slight narrowing of the peak as the t/a ratio is increased. Fig. 23 (b) shows a rapid reduction in peak height as the t/a approaches the symmetric case of t/a = 0.5. This is caused by

the impossibility of even-order terms occurring in the Fourier expansion of the fringing fields when the grating is symmetric (Fig. 19).
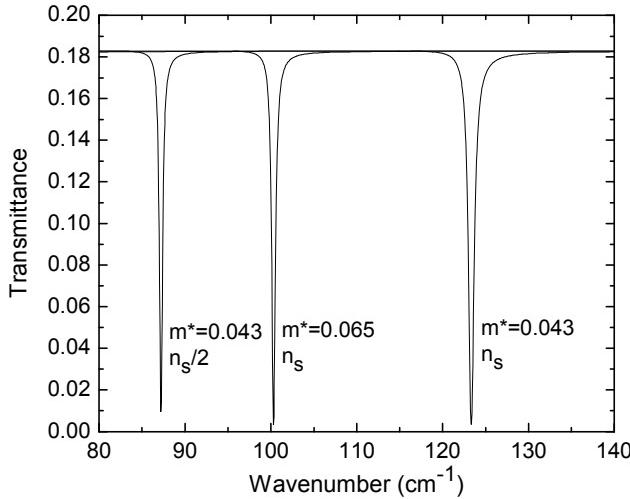

Fig. 21. Simulated transmittance for the device of this work showing effects of changes to effective mass and 2-deg sheet charge density.
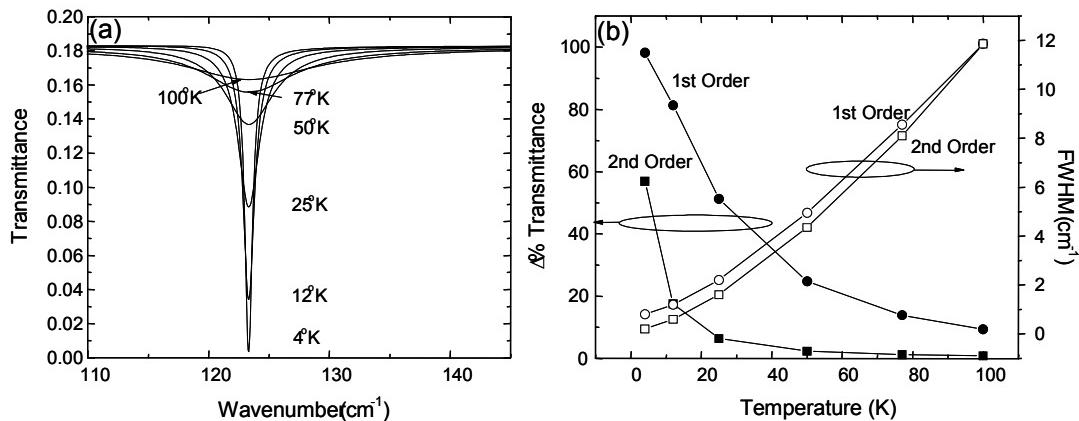

Fig. 22(a). Simulated transmittance showing effects of temperature on both percent change in transmittance and linewidth. (b) Details of similar measurements for both first and second order plasmon resonances.

The calculated spectra suggest that plasmon resonances can be generated from incident radiation having a short wavelength limit of roughly 26 μm. These resonances will alter the transmission through the device producing a voltage variable band-blocking filter of FWHM less than 1 cm^{-1} at 4K and 5 cm^{-1} at 50 K. Alternatively, because plasmons influence the 2-deg channel conductance, the device can be operated as a frequency-selective photo-conducting transducer. Fig. 24 illustrates the calculated

voltage tunability where device transmittance is plotted at various gate biases. For this and all subsequent figures a *t/a* ratio of 0.65 and a zero bias 2-deg sheet charge of 2.4 x 10^{12} cm^{-2} are used. As can be seen, a voltage swing of 0.55 volts allows for detection of incident radiation from roughly 2.75 THz to 3.75 THz. In principle, increasing the grating period can shift this 1 THz detection band for the given semiconductor layer structure to any desired lower frequency.
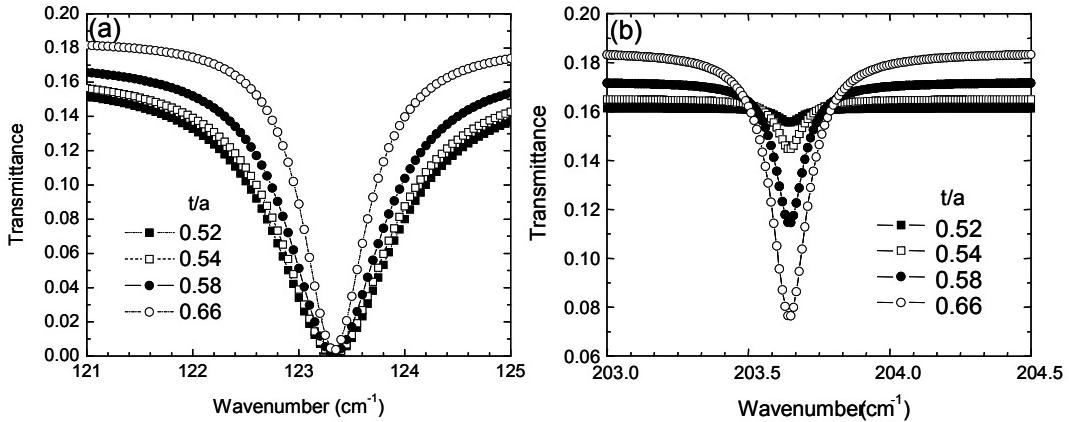

Fig. 23. Calculated effect of changing grating duty *t/a* on the (a) first order and (b) second order plasmon induced transmission spectrum.
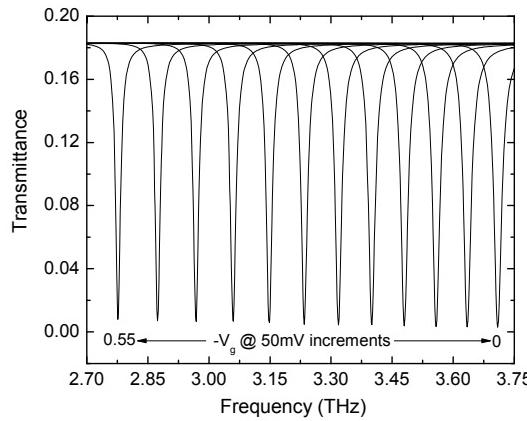

Fig. 24. Resonance tuning with gate voltage**.**

Two modes of operation for spectroscopy with the considered device can be envisioned. As a voltage tunable band-blocking filter before a broad band detector, it can be useful for spectroscopy of narrow-band molecular emission. In this mode, the

detector output Γ is proportional to the product of the incident spectral density $I(\omega)$ and filter transmittance T, integrated over the detector bandwidth

$$\Gamma(\omega, V_g) = \int I(\omega) T(\omega, V_g) d\omega .$$ (33)

Fig. 25 (a) is a simulated emission spectrum with two resonance peaks separated by 4 cm^{-1}, with each peak having a FWHM of 0.4 cm^{-1}. Figure 25 (b) shows a simulation of the detector response as a function of temperature and illustrates how the increased FWHM of the device transmittance at elevated temperatures effects overall spectral resolution. It is interesting to note, that even a 4 cm^{-1} peak separation can still be resolved at a temperature as high as 50 K, which is in range of compact closed cycle Stirling refrigerators. A drawback of this mode of spectroscopy is that radiation blocked by the filter but within the detector bandwidth adds noise and reduces dynamic range. This effect can be minimized through the use of a prefilter to limit the spectral response to a narrow band.
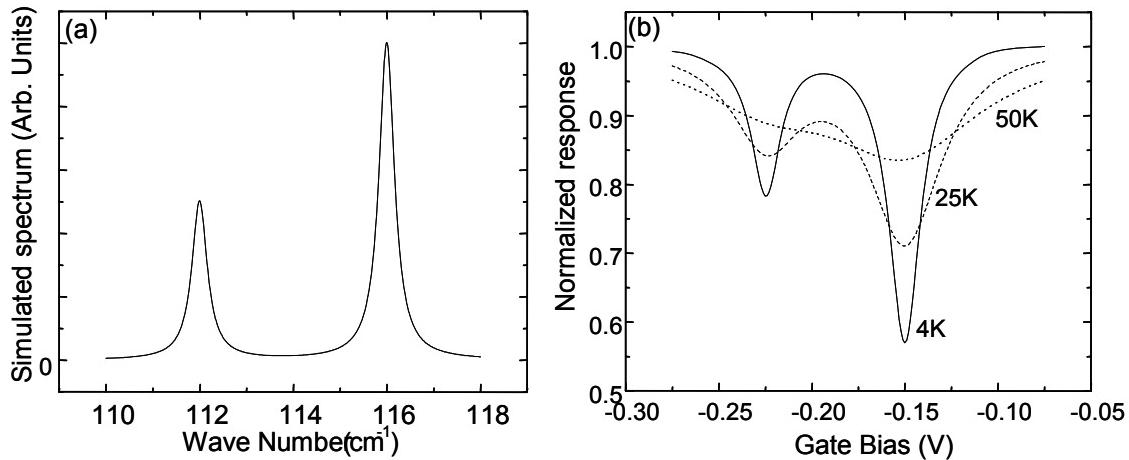

Fig 25 (a) Simulated incident radiation spectrum used to simulate (b) response of detector when the device of this work is used as a tunable notch filter.

A potentially cleaner mode of operation is as a voltage tunable detector where absorbed radiation within the plasmon resonance is sensed as a change in the source/drain current of the device. Though this effect has been observed in the AlGaAs materials system [9,10], this mode is still somewhat speculative because the mechanism of Plasmon-conductance interaction is unknown, and the sign, linearity, temperature

dependence, and magnitude of the response all remain uncertain. These questions will be investigated experimentally.

References

1. M. A. Ordal, R. J. Bell, R. W. Alexander, Jr., L. L. Long, and M. R. Querry, "Optical properties of fourteen metals in the infrared and far infrared: Al, Co, Cu, Au, Fe, Pb, Mo, Ni, Pd, Pt, Ag, Ti, V, and W," Appl. Optics 24, 4493 (1985).

2. J. T. van Wijngaarden, E. Verhagen, A. Polman, C. E. Ross, H. J. Lezec, and H. A. Atwater, "Direct imaging of propagation and damping of near-resonance surface Plasmon polaritons using cathodoluminescence spectroscopy," Appl. Phys. Lett. 88, 221111 (2006).

3. Andreas Otto, "Excitation of nonradiative surface plasma waves in silver by the method of frustrated total reflection," Z. Physik 216, 398 (1968).

4. E. Kretschmann, "The determination of the optical constants of metals by excitation of surface plasmons," Z. Physik 241, 313 (1971).

5. Heinz Raether, Surface Plasmons on Smooth and Rough Surfaces and on Gratings (Springer, Berlin, 1986), Appendix

6. J. T. van Wijngaarden, E. Verhagen, A. Polman, C. E. Ross, H. J. Lezec, and H. A. Atwater, "Direct imaging of propagation and damping of near-resonance surface Plasmon polaritons using cathodoluminescence spectroscopy," Appl. Phys. Lett. 88, 221111 (2006).

7. R. H. Ritchie, "Plasma losses by fast electrons in thin films," Phys. Rev. 106, 874 (1957).

8. S.J. Allen, D.C. Tsui, R. A. Logan, "Observation of the two-dimensional Plasmon in silicon inversion layers," Phys. Rev. Lett. **38**, 980 (1977).

9. E.A. Shaner, Mark Lee, M.C. Wanke, A.D. Grine, J.L. Reno and S.J. Allen, "Single-quantum-well grating-gated terahertz Plasmon detectors," Appl. Phys. Lett. **87**, 193507 (2005).

10. X.G. Peralta, S.J. Allen, M.C. Wanke, N.E. Harff, J.A. Simmons, M.P. Lilly, J.L. Reno, P.J. Burke and J.P.Eisenstein, "Terahertz photoconductivity and Plasmon modes in double-quantum-well field-effect transistors," Appl. Phys. Lett, **86**, 1627 (2002).

11. P.M. Smith, S.-M. J. Liu, M.-Y. Kao, P. Ho, S.C. Wang, K.H. Duh, S.T. Fu and P.C. Chao, "W-band high efficiency InP-based power HEMT with 600 GHz f_{max}," IEEE Microwave and Guided Wave Lett. **5**, 230 (1995).

12. R. Lai, M. Barsky, T. Huang, M. Sholley, H. Wang, Y.K. Kok, D.C. Streit, T. Block, P.H. Liu, T. Gaier, and L. Samoska, "An InP HEMT MMIC LNA with 7.2-dB gain at 190 GHz," IEEE Microwave and Guided Wave Lett. **8**, 393 (1998).

13. M. Littlejohn, K. Kim, and H.Tyan, "High-field transport in InGaAs and related heterostructures", in Properties of Lattice-Matched and Strained Indium Gallium Arsenide, P. Bhattacharya, ed (No.8 in EMIS Data reviews series IEEE INSPEC, 1993).

14. L. A. Cury, J. Beerens, J. P. Praseuth, "Dependence of conduction-band effective mass on quaternary alloy composition of $(In_{0.52}Al_{0.48}As)_z(In_{0.53}Ga_{0.47}As)_{1-z}$ lattice matched to InP," Appl. Phys. Lett. **63**, 1804 (1993).

15. J.-H. Huang, T. Y. Chang, and B. Lalevic, "Measurement of the conduction-band discontinuity in pseudomorphic $In_xGa_{1-x}As/In_{0.52}Al_{0.48}As$ heterostructures," Appl. Phys. Lett. **60**, 733 (1992)

16. A. V. Muravjov, H. Saxena, R. E. Peale, C. J. Fredricksen, O. Edwards, and V. N. Shastin, "High-power terahertz p-Ge laser with injection seeding," to be published (2007).

17. L. Zheng, W. L. Schaich, and A. H. MacDonald, "Theory of two-dimensional grating couplers, Phys. Rev. B **41**, 8493 (1990)].

18. C. Kittel, Introduction to Solid State Physics, 2nd Ed. (John Wiley & Sons, New York, 1956), p. 352.

19. Y. T. Dai, Y. F. Chen, and I. Lo, Effects of band offset and nonparabolicity on the effective mass of two-dimensional electron gases in modulation-δ-doped $Ga_{0.47}In_{0.53}As$-based heterostructures," Phys. Rev. B **55**, 5235 (1997).

20. K. Hofmann, B. Spangenberg, M. Luysberg, and H. Kurz, "Properties of evaporated titanium thin films and their possible application in single electron devices," Thin Solid Films **436**, 168 (2003).

List of Acronyms

CL	Cathodoluminescence
FWHM	Full Width Half Maximum
HEMT	High Electron Mobility Transistors
SPP	Surface Plasmon Polaritons